Explicit calculation of natural aeration using a Volume-of-Fluid model

Pedro Lopes[a,b,*], Gavin Tabor[c], Rita F. Carvalho[a,b], Jorge Leandro[a,b]

[a]Department of Civil Engineering, University of Coimbra, Portugal
[b]MARE - Marine and Environmental Sciences Centre, University of Coimbra, Portugal
[c]College of Engineering, Mathematical and Physical Sciences, University of Exeter, United Kingdom

Abstract

Accurate prediction of the air-entrainment process in air-water two-phase turbulent flows is one of the most computationally challenging subjects under current investigation in hydraulic engineering. An ideal numerical model for air-entrainment needs to be accurate and fast in the definition of a macroscopic interface and simultaneously precise enough to take into account the formation of bubbles through the free-surface, their transport and their natural interactions: bubble-bubble and bubble-fluid. The problem is made more complex by the strong coupling between mesh and solution exhibited by interface capturing schemes which are commonly used for such problems. This paper examines numerical and modelling aspects of the entrainment process for two canonical cases; the 2D dam break and 3D circular plunging jet cases. We start by investigating the capacities of a Volume-of-Fluid based model to detect the free-surface and predict the velocities inside the water phase, examining the effect of coarsening and refining the mesh on the prediction of the interface location. A reformulated explicit term is used to detect bubble formation and air-entrainment at the free-surface, without the need of a calibration process and adapted to run together with Volume-of-Fluid models. The results obtained with this new approach are further compared with similar cases in the literature in terms of bubble formation and free-surface wave's amplitude. The correct definition of the free-surface was found to be strongly dependent on the mesh refinement in a way that has very significant implications for the development of air-entrainment modelling.

Keywords: Air-entrainment, Air-water two-phase flow, Sub-grid explicit model, Volume-of-Fluid

1. Introduction

Air-entrainment occurs in most turbulent free-surface flows in nature resulting in a dispersed two-phase flow below the surface with a complex turbulent mixture structure, where compressibility and density are important physical properties affecting the air-entrainment and transport characteristics. The accurate prediction of air-entrainment is a very ambitious goal for most Computational Fluid Dynamics (CFD). The air-water interface is very unstable and the length scales of turbulence range from those influenced by the bubbles and surface tension (order from microns to

*Corresponding author at: Hydraulic, Water Resources and Environment Laboratory, Room S.H.4.6, Department of Civil Engineering - Polo 2 University of Coimbra, Rua Luís Reis Santos, 3030-788 Coimbra, Portugal; Tel.: +351 239 797 228.

Email addresses: `pmlopes@student.dec.uc.pt` (Pedro Lopes), `G.R.Tabor@exeter.ac.uk` (Gavin Tabor), `ritalmfc@dec.uc.pt` (Rita F. Carvalho), `leandro@dec.uc.pt` (Jorge Leandro)

millimetres) to those of the mean flow (order of meters). The simulations should be able to work on a coarse grid in order to simulate the mean flow behaviour, the free-surface position and all the similar large length scales (LLS), whilst at the same time being sufficiently detailed to model the transport of the bubbles of gas within the flowing fluid and simulate important phenomena as bubble formation, breakup, coalescence and collision, which take place on small length scales (SLS).

In CFD, Volume-of-Fluid (VOF) [16] and Level-Set (LS) [32] based models are typically used to capture the interface between two fluids, solving a single set of Navier-Stokes equations representing both air and water, together with an indicator function propagated by an advection equation. These interface models are widely used for many free-surface flows with macroscopic interfaces and LLS systems, as in vertical plunging jets [17, 24, 28]. Direct Numerical Simulations could simulate all aspects of the entrainment process right down to the subsequent dynamics of the bubbles; however this would be incredibly time-consuming and, in some cases, the application of VOF method to dispersed phases could lead to a non-physical interpretation of bubbles or droplets [7]. Instead, for a realistic mesh resolution the representation of the entrained air (SLS system) can be accomplished by the inclusion of an Eulerian dispersed phase model with a second set of equations representing the dynamics of the bubbles. Different approaches that follow this idea can be found in the literature. The model of Cerne et al. [7] blends the VOF interface tracking with a two-fluid model formulation [11]. In this model, in zones where the phase separation are clear and where just one fluid is present, the two-fluid model is switched off and a single set of Navier-Stokes equations together with the VOF method is solved instead. A criterion based on the local dispersion of the interface is used to switch between the two formulations, however, the accuracy of the results has exhibit a strong dependence on the value of this threshold which goes against the essence of a blending model. To overcome the dependency of the dispersion threshold, Yan and Che [39] introduced a unified solution framework for coupling VOF with a two-fluid model. The idea was to blend the two formulations ensuring the conservation of all three phases; i.e. when the LLS of air are present (phase2), the interface tracking model is activated; then when the LLS are absent from the cell, the two-phase model is used to solve for the local characteristics of the fluids (phase1 for water and phase3 for bubbles). The model shown to be efficient for the simulation of a rising bubble and a swarm of bubbles in a vertical pipe. However, volume fraction conservation when the three phases are present is not guaranteed, with particular losses occurring for phase2. Wardle and Weller [36] introduced in OpenFOAM® a hybrid formulation based on the combination of an Eulerian multifluid framework (to solve the SLS) with an interface capturing method using VOF (to solve the LLS), along with a switching function based on the work of Cerne et al. [7]. Shonibare and Wardle [33] extended this hybrid model to deal with variable bubble size using the reduced population balance method and applied it to a vertical plunging jet. A similar conceptual approach to the last was implemented by Marschall and Hinrichsen [25] in OpenFOAM® for solely two-phase flows. Hänsch et al. [14] extended the inhomogeneous Multiple Size Group (MUSIG)-approach by adding a continuous gas phase in order to solve simultaneously in the same domain, dispersed and continuous gas phases. The transition between the two was modelled by the "clustering method" that utilises an additional interfacial force applied to the Eulerian multifluid framework. The solutions were verified for the case of plunging jets. Yet another

type of subgrid models combine an interface model (VOF/LS) with the two-phase flow formulation by including a source term to detect the air formation at the free-surface [15, 22, 23]. Source terms at the interface relate the rate of bubble formation to surface flow properties such as local turbulence and the size of interface waves.

A typical experiment in which air-entrainment has been observed and extensively studied is the plunging jet [1, 2, 4, 8, 10, 18, 29, 31]. Plunging jets are efficient mechanisms to dissipate energy, and in doing so produce and transport significant quantities of bubbles through the body of the water. Practical examples of plunging jets include dam spillways and plunge pool stilling basins, waste-water treatment, oxygenation of bioreactors and river re-oxygenation. Air-entrainment in the pool depends upon the jet impact, the physical properties of air and water, the jet diameter, the free falling distance between the jet and the pool, and the jet turbulence. At the intersection point of the jet and the water, free-surface instabilities are the reason for air-entrainment when the jet impact velocity exceeds a characteristic velocity or onset velocity [8]. Slightly above the onset velocity, the air entrains in the form of individual bubbles and small pockets. At the impact point, the free-surface is observed to assume a shape which balances the forces between both sides of the interface. With increased liquid velocity at the jet impact zone, the local stress is increased, and small cavities are formed and pulled bellow the free surface. Deeper into the pool, these cavities decrease in radius but continue balancing the surface forces. A critical condition is reached where either (a) a steady balance of forces can no longer be maintained or (b) the inferior end of the cavity or the free-surface is disrupted by disturbances at the free jet stream and/or on the pool. The result is the sequential generation of small bubbles or air pockets below the free surface. In this case, the rate of air-entrainment is very small and challenging to measure with common intrusive probes. At higher jet velocities, a substantial air pocket or sheath is formed at the periphery of the jet below the free surface; this air pocket is unstable and its breakup forms the entrained air bubbles which are then the subject of transport within the body of the water [4].

This paper proposes a reformulated explicit term for bubble formation that is independent of calibrating factors by using a renewed formula for surface wave's amplitude. The explicit term was included in the well validated *interFoam* VOF solver from the OpenFOAM® toolkit to accurately predict the interface position [19, 20, 21]. An interface location coefficient is necessary for this coupling. This study represents a starting point for the development of a VOF-based model with a modelled closure to represent the entrained air. Section 2 develops the equations behind the numerical model along with the interface location technique and the air-entrainment term. Section 3 presents the results and their discussion for two canonical test cases; a 2D dam break case and a 3D plunging jet. Finally, section 4 presents conclusions.

2. Numerical Model

2.1. General concepts

Interface capturing models such as the VOF model (implemented in the OpenFOAM® toolkit as *interFoam*) represent the free-surface dynamics of the two phases in terms of single phase-weighted velocity and pressure fields,

governed by a single set of mass and momentum equations. For a system of isothermal, incompressible and im-
miscible two-phase flow, the Reynolds averaged equations for mass conservation and momentum are written in their
conservative form:

$$\nabla \cdot \mathbf{U} = 0 \tag{1}$$

$$\frac{\partial \rho \mathbf{U}}{\partial t} + \nabla \cdot (\rho \mathbf{U}\mathbf{U}) = -\nabla p^* + \mathbf{g} \cdot \mathbf{x}\nabla\rho + \nabla \cdot \boldsymbol{\tau} + \mathbf{f} \tag{2}$$

where ρ ($kg\ m^{-3}$) is the fluid local density, $\mathbf{g}$ ($m\ s^{-2}$) the gravitational acceleration, $\mathbf{U}$ ($m\ s^{-1}$) the velocity vector,
$\boldsymbol{\tau}$ (Pa) the shear stress tensor, p^* (Pa) a modified pressure adopted by removing the hydrostatic pressure ($\rho\mathbf{g} \cdot \mathbf{x}$)
from the total pressure and $\mathbf{f}$ ($kg\ m^{-2}s^{-2}$) the volumetric surface tension force. It is important to note that in interface
capturing models, the velocity vector $\mathbf{U}$ acts as a shared velocity of the two fluids, i.e. $\mathbf{U} = \mathbf{U}_{f1} = \mathbf{U}_{f2}$, rather than in
mixture models where $\mathbf{U}_{fk}, k = \{1, 2\}$ can assume different magnitudes.

The decomposition of the viscous stress term is given by the Stokes's stress constitutive equation (Eq. 3) where
μ ($kg\ m^{-1}s^{-2}$) is the dynamic viscosity.

$$\nabla \cdot \tau = \nabla \cdot [\mu(\nabla\mathbf{U} + (\nabla\mathbf{U})^T)] = \nabla \cdot (\mu\nabla\mathbf{U}) + (\nabla\mathbf{U}) \cdot \nabla\mu \tag{3}$$

Together with the previous equations, *interFoam* uses the VOF technique [16] to capture the interface between the
two fluids by solving a transport/advection equation (Eq. 4). Basically, at each cell of the domain we define an alpha
(α) value representing the fraction of the volume of the fluid in that cell [6, 34]. Cells completely filled with fluid
1 ($f1$) will be represented by $\alpha = 1$ and cells filled with fluid 2 ($f2$), by a value $\alpha = 0$. The interface is localised
to the cells where α is intermediate between these two values. The advection equation also includes an interfacial
compressive term to confine this interface region into as small a region of space as possible (the last term on the l.h.s.
of Eq. 4) [3, 37], rather than using interface reconstruction schemes [30].

$$\frac{\partial\alpha}{\partial t} + \nabla \cdot (\alpha\mathbf{U}) + \nabla \cdot [\mathbf{U}_c\alpha(1 - \alpha)] = 0 \tag{4}$$

The term $\alpha(1 - \alpha)$ ensures that the compressive term is calculated just at the interfacial cells of the domain, while
C_α is a binary coefficient that activates ($C_\alpha = 1$) or deactivates ($C_\alpha = 0$) the interface sharpening term. The source
term also includes the compressive velocity ($\mathbf{U}_c$) that acts as a velocity perpendicular to the interface and is written as:

$$\mathbf{U}_c = C_\alpha|\mathbf{U}|\frac{\nabla\alpha}{|\nabla\alpha|} \tag{5}$$

It is worth emphasising that the interface is merely being localised within the volume of space for which $0 < \alpha < 1$.
For simplicity it is often taken that the interface is represented in post-processing by the isosurface $\alpha = 0.5$, but strictly
speaking this is simply an assumption, one which we wish to explore in the present work.

When α assumes values between 0 and 1, the physical properties of the two-fluid mixture are defined as a weighted average of two fluid properties:

$$\rho = \alpha\rho_{f1} + (1 - \alpha)\rho_{f2} \tag{6}$$

$$\mu = \alpha\mu_{f1} + (1 - \alpha)\mu_{f2} \tag{7}$$

The volumetric surface force function is explicitly estimated by the Continuum Surface Force (CSF) model (Eq. 8) developed by Brackbill et al. [5] where σ $(kg\ s^{-2})$ is the surface tension and κ (m^{-1}) is the surface curvature calculated as $\kappa = \nabla \cdot (\nabla\alpha/|\nabla\alpha|)$.

$$\mathbf{f} = \sigma\kappa\nabla\alpha \tag{8}$$

The turbulent kinetic energy (k) and rate of energy dissipation (ε) are calculated using the realizable $k-\varepsilon$ turbulence model, with the effective dynamic viscosity (μ) being given by a sum of molecular viscosity (ν) and turbulent viscosity (ν_t) ($\mu = \rho(\nu_t + \nu)$). The choice of the realizable $k - \varepsilon$ is based on its known ability to accurately predict the spreading rate of both planar and round jets [13, 40]. This turbulent model is also superior to the standard $k - \varepsilon$ model for the simulation of flows involving rotation, boundary layers under strong pressure gradients, separation and recirculation. The realizable $k - \varepsilon$ also requires less computational time than Re-Normalisation Group (RNG) $k - \varepsilon$ which was derived to deal with the swirl effect on turbulence [13].

2.2. Bubble formation

The air-entrainment process is described by the inclusion of a function E_g $(m^{-3}s^{-1})$ which describes the rate of bubble generation at the free-surface. It is calculated at the end of each time-step and does not change any convergence process within the standard solver. The formulation of this variable follows closely the work of Ma et al. [23], who represent it as:

$$E_g = \left\langle \frac{\partial \mathbf{U_n}}{\partial \mathbf{n}} \right\rangle \frac{a}{\phi_{ent}V_g} \tag{9}$$

where $\mathbf{U_n}$ is the normal velocity component to the free-surface, a (m) is the amplitude of the cavities formed at the free-surface (Fig. 1), V_g (m^3) is the volume of a sphere calculated assuming an averaged bubble diameter and ϕ_{ent} (m) is the interface thickness, given by $\phi_{ent} = 0.05L$, where L (m) is a characteristic linear dimension (equal to the pipe diameter for pipe flow or the hydraulic diameter when dealing with river systems). The symbols $\langle \rangle$ are used to turn the normal derivative zero if its value is less than zero:

$$\langle f(x) \rangle = \begin{cases} f(x) & , \ f(x) > 0 \\ 0 & , \ f(x) \leq 0 \end{cases} \tag{10}$$

A rough way to predict the volume fraction occupied by the bubble phase at each cell can be done by $E_{g,frac} = E_g V_g \Delta t$, where Δt (s) is the computational time step. This neglects the advection and diffusion terms of the void fraction conservation and transport at the free-surface, however, when the velocities are small, it can provide a good first impression of void fraction magnitude.

In this work and according to Ervine and Falvey [12], the amplitude of the surface disturbances (a) is considered as having the same order of magnitude as the radius of the turbulent eddies at the free-surface (l'). From here, we obtain:

$$a = l'/2 = C_\mu^{3/4} \frac{k^{3/2}}{2\varepsilon} \tag{11}$$

where C_μ is a turbulence model constant which in the $k - \varepsilon$ model theory assumes the value 0.09 [27, 35]. Similar criteria is used by Hirt [15] to calculate surface disturbances at free-surface in the CFD commercial code Flow-3D®. In the model of Ma et al. [23], the amplitude of the surface disturbances (a) is calculated as $a = C_{ent} \, k/g$, where C_{ent} is a constant that needs to be calibrated for each case.
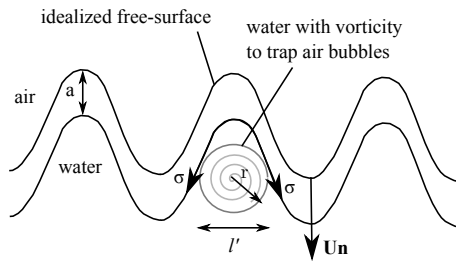

Figure 1. Free-surface with physical parameters used. Adapted from Ervine and Falvey [12].

2.3. Interface location

The location of the air-entrainment in our VOF model does not follow the same criteria as in work from Ma et al. [23] (which uses LS methods). In LS, the interface can either be located by assuming a certain threshold for interface thickness, or by limiting the velocity to some threshold value. However, in VOF models, the interfacial structure can only be detected by the change of volume fraction or by its gradient, as for example in the the algebraic equation formulated by Hänsch et al. [14]. In this work, E_g is calculated using a similar criterion as used for the compressive term, i.e. by multiplying the last by the function $\phi_{FS} = 4\alpha(1-\alpha)$. This will work as a masking function, which returns 0 when calculated in cells away from the free-surface and 1 at the interface. From the fact that this coefficient uses α to detect the free-surface, it is fairly essential keep the interface confined to a small number of cells possible, and from this we see the need of a mesh dependence study.

3. Results: Example cases

3.1. 2D Dam-break

The example presented here is the benchmarking 2D dam-break case without obstacle. This case is used by many other authors to show the capabilities of free-surface models and of interest for this work as it can exhibit several possible zones of natural aeration of the flow and the interface location. A static water column is initially held against the left wall by a vertical gate as shown in Fig. 2. On removing the gate, the water column collapses and the resulting slosh hits the right wall before returning in the form of a small propagating wave.
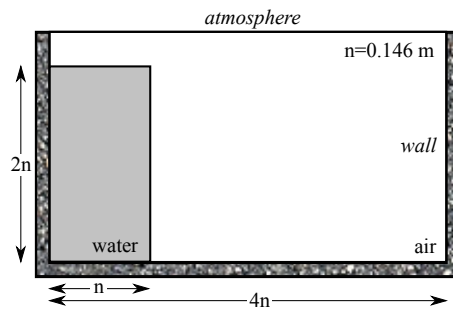

atmosphere

n=0.146 m

wall

2n

water   air

n   4n

Figure 2. 2D dam-break domain.

Numerical simulations are performed in four different meshes: 16×16, 32×32, 46×46 and 64×64 cells. The fluid properties were chosen to represent the physical values of water and air at 15°C. Surface tension is set to 0.072 $kg\ s^{-2}$, the averaged bubble radius (r_b) is 0.002 m and $\phi_{ent} = 0.05n = 0.0071\ m$, where n stands for the water column width (Fig. 2). The domain is bounded by walls with the exception of the top one that represents the atmosphere. The pressure at the walls is given by Neumann boundary conditions (BC), whilst the velocity is set to no-slip (Dirichet-BC).

Figure 3 presents snapshots of the free-surface position for $t = 0.1$, 0.3, 0.7 and 1.0 s for finer mesh. Figure 3a shows the ϕ_{FS} function and Fig. 3b the values of the terms E_g and $E_{g,frac}$. Figure 4 demonstrates the influence of changing the mesh size on the free-surface position for $t = 0.8$ s. Again, Fig. 4a shows the ϕ_{FS} function and Fig. 4b the values of the terms E_g and $E_{g,frac}$.

The function used to detect the free-surface has demonstrated excellent accuracy throughout the simulation time even when a large cavity is formed inside the fluid (Fig. 3a4). One second after the collapse of the water column (Fig. 3b1), due to the friction with the bottom wall, air is forced to enter from the bottom, where the term E_g assumes high values. High values of air-entrainment can also be seen in the zone where the water collides with the right wall (Fig. 3b2) and on its way back in the area where a small cavity of the breaking wave is formed (Fig. 3b3). The mesh influence study show a large difference between meshes 16×16 and 32×32 cells both for ϕ_{FS} and E_g values. The free-surface in the last three finer meshes have a similar shape, whereas the maximum values of E_g are on the order of 4×10^7 in the mesh with 32×32 cells (Fig. 4b2) and of the order of 5×10^7 for 46×46 and 64×64 cells (Fig. 4b3 and
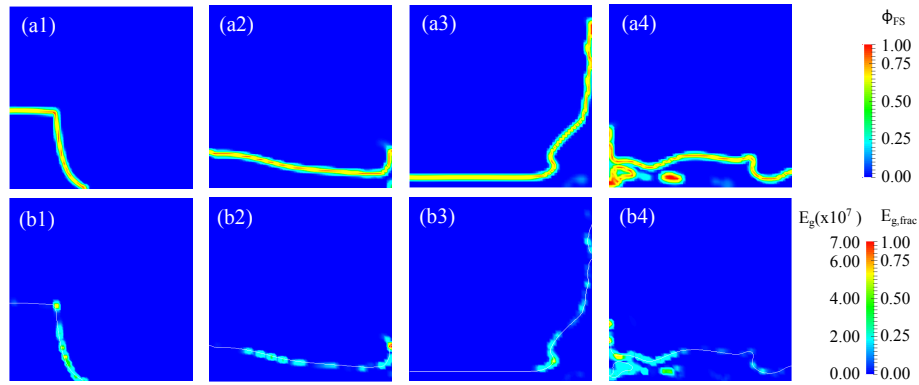
Figure 3. Dam-break process for the time steps $t = 0.1, 0.3, 0.7$ and $1.0 s$ using the finest mesh (64×64 cells). Top images are photographs of the experiment, middle figures (a) show the function to detect the free-surface position (ϕ_{FS}) and bottom figures (b) show the bubble formation term (E_g) and its volume fraction on the cells ($E_{g,frac}$).
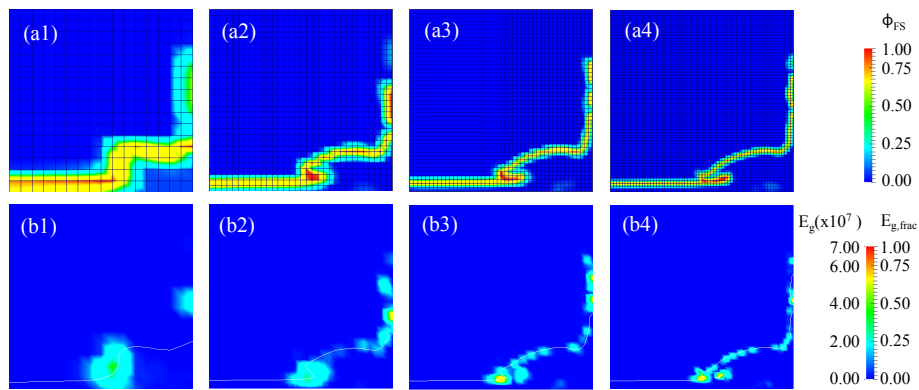

Figure 4. Mesh influence study of dam-break case at $t = 0.8 s$. From the left to right the meshes are: 16×16, 32×32, 46×46 and 64×64 cells. Top figures (a) show the function to detect the free-surface position (ϕ_{FS}) and bottom figures (b) show the bubble formation term (E_g) and its volume fraction on the cells ($E_{g,frac}$).

1 Fig. 4b4). This shows that, even with the decreasing of the mesh size, the values of E_g are quasi mesh independent,

2 although its spacial location is sensible to the grid size.

3 *3.2. 3D vertical plunging jet*

4 The 3D computational domain represents a part of the experimental apparatus used by Chanson and Manasseh

5 [9], schematically represented in Fig. 5. This experimental work provides extensive data on void fraction and bubble

6 count rate inside the water, which despite not being relevant in this work, will be useful to compare the results when a

7 full air-entrainment model is completed. The simulation of a 3D domain rather than a 2D domain allows us to better

8 represent all the flow structures across the interface which are manifestly 3D structures. Also, comparisons to the 3D

9 model of Ma et al. [22] in terms of E_g values and later for void fractions can be done clearly and without constraints

10 (note that Ma et al. [22] applied their model to the same case in their study).

11 A plunging jet of clean water is ejected from a $d_0 = 0.025$ m diameter nozzle, into a pool of stationary water. The

12 distance between the water surface and the nozzle is constant and equal to $x_1 - x_0 = 0.1$ m. The impact velocity of

13 the jet at the pool is $U_1 = 3.5$ m s^{-1}. Velocity profiles are obtained at different horizontal planes from $0.8d_1$ (m) to

14 $10.0d_1$ (m) below the initial pool free-surface, where d_1 is the jet diameter at the impact zone ($d_1 \approx 0.024$ m) and

15 r_1 the jet radius ($r_1 \approx 0.012$ m). To investigate the impact of mesh resolution on the solution, three different grids

16 with different mesh resolutions were generated and their characteristics summarized in Table 1. In order to decrease

17 the computational time, instead of using spatially uniform meshes, three zones with different grid sizes are created as

18 defined in Fig. 5.

	cell length, Δx (m)			N.Cells	N.Proc.	Time (s)
	jet and surface (Z1)	centre-bottom (Z2)	lateral (Z3)			
Coarse grid (*G*0.005)	0.005	0.005	0.005	84 192	16	1963
Medium grid (*G*0.0025)	0.0025	0.0025	0.005	521 124	16	39 891
Fine grid (*G*0.00125)	0.00125	0.0025	0.005	2 104 460	16	281 073
Finnest grid (*G*0.0008)	0.0008 - 0.00125*	0.0025	0.005	2 458 835	32	284 242

Table 1. Grid characteristics to demonstrate the mesh dependency. Zones Z1, Z2 and Z3 are represented in Fig. 5. *In this case, cells with 0.0008 m edges were placed just on the intersection between jet and pool.

19 The initial conditions are set as represented in Fig. 5. The pool is filled with stationary water ($U = 0$ m s^{-1}) to a

20 constant depth. A cylindrical column of water with a fixed inlet velocity is used to represent the jet. In order to get fast

21 convergence of the solution and computational stability the air velocity in the vicinity of the jet is set equal to the jet

22 velocity. Four different boundary conditions (BC) are used in this simulation as shown in Fig. 5. The velocity at the

23 *inlet* is calculated based on the jet impact velocity using Bernoulli's principle, $U_0 = \sqrt{U_1^2 - 2g(x_1 - x_0)} = 3.21$ m s^{-1}.

24 The *atmosphere* just allows the air to leave the domain by setting U as dependent on pressure with total pressure set

25 as zero. The *lateral* boundaries have Neumann-BC for α, p equal to hydrostatic pressure and non-slip Dirichet-BC

26 for U. For the *bottom* boundary the hydrostatic pressure is set to $\rho_{f1} g(x_{bottom} - x_1) = 3915.2$ Pa and Neumann-BC are
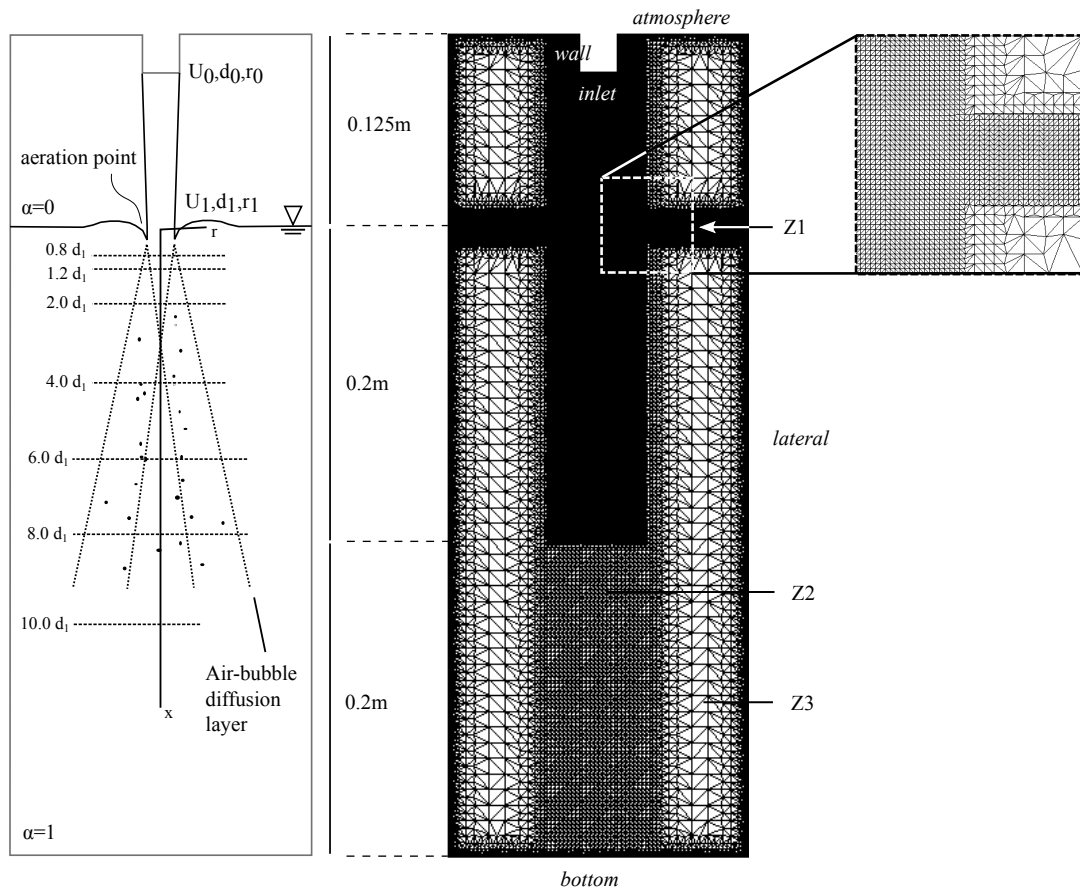
Figure 5. Vertically-centred slice of the computational domain for the 3D circular plunging jet problem. The mesh presented corresponds to G0.00125 (Table 1).

used for the remaining variables. In order to verify the correct application of these boundary condition, we simulated with the coarser mesh the full experimental domain and verified that the results in terms of U, p and α in the zone close to the jet agreed with those calculated on the smaller domain.

The k, ε and ν_t variables at the *inlet* are calculated by:

$$k_0 = \frac{3}{2}(U_0 I_0)^2 = 0.000235 \ m^2 s^{-2} \tag{12}$$

$$\varepsilon_0 = C_\mu \frac{k_0^{3/2}}{l_0} = 0.000371 \ m^2 s^{-3} \tag{13}$$

$$\nu_{t,0} = C_\mu \frac{k_0^2}{\varepsilon_0} = 1.3416 \times 10^{-5} \ m^2 s^{-1} \tag{14}$$

where U_0 ($m \ s^{-1}$) is the mean flow velocity at jet inlet; I_0 (%) the turbulent intensity at jet inlet, set as 0.39 % (value from the experiment of Chanson and Manasseh [9]) and l_0 (m) the length scale at jet inlet, in this study calculated as $l_0 = 0.035 \ d_0$ (m). On the remaining boundaries k_0, ε_0 and $\nu_{t,0}$ are defined as Dirichlet-BC. The fluid properties were chosen based on the physical values of water and air at 15°C. Surface tension is set to 0.072 $kg \ s^{-2}$, bubble radius (r_b) is 0.00175 m and $\phi_{ent} = 0.0012 \ m$. The simulation ran with the extra term activated from the beginning. A steady-state solution was acquired after 6500 time iterations with an averaging time step of 0.0001 s for the simulation with coarser mesh, which gives a final time of about 0.65 s. This state was identified from the criteria that the residuals of k, ε and p, and the volume fraction on the domain were constant in time. The averaged values from the last 0.1 s were used to plot the results. Maximum Courant number and maximum Courant for α are both defined to 0.5.

3.2.1. Radial velocity profiles

The liquid velocity plays a key role in the transport of bubbles into the fluid. This therefore represents a good variable with which we can validate the solution and demonstrate grid independence. In order to prove this, in this section, the computed radial distribution of liquid velocity is presented. Figure 6 shows the dimensionless radial velocity profiles (U/U_1) on the pool depths of $x = 0.8d_1$, $1.2d_1$ and $2.0d_1$ for the four meshes presented. These three profiles were chosen here because these were the positions where Chanson and Manasseh [9] measured experimentally the air concentration profiles.

From the data in Fig. 6, it can be seen that the velocity has the maximum value at the jet centreline and tends to zero away from the centre. For a free jet in air, the greater the distance from the jet inlet, the lower and wider the velocity profile becomes, eventually assuming the universal shape of a Gaussian curve [26]. However, for a jet impacting a pool it is also known that the profiles closer to jet impact zone are affected by the abrupt decreasing of the velocity from its maximum value to zero. This situation is clearly visible in the results of the finer mesh (Fig. 6). The velocity on the jet axis was equal to 3.5 $m \ s^{-1}$ ($U/U_1 = 1.0$), and this value remained constant until a distance equal to the radius of the jet. After reaching a distance of $1.0r/r_1$, the velocity passed from this maximum to roughly zero in about $0.25r/r_1$. On the coarser meshes, numerical viscosity smooths the profile; the axis velocity remains correct
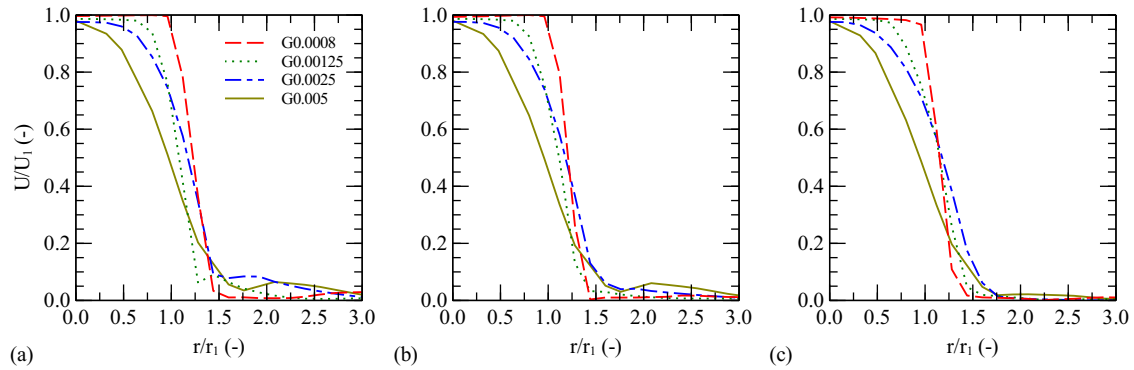
Figure 6. Liquid velocity for pool depths (a) $x = 0.8d_1$ (*m*), (b) $x = 1.2d_1$ (*m*) and (c) $x = 2.0d_1$ (*m*). $U_1 = 3.5$ *m* s^{-1}, $d_1 = 0.024$ *m* and $r_1 = 0.012$ *m*.

and the curves tends to zero velocity at similar values of $r/r_1 \approx 1.5$, but the shape of the curve between these extremes is significantly affected, with a smoother shape for the coarser meshes indicating a reduction of velocity inside the jet ($r/r_1 < 1.0$). On the finest mesh the jet flow remains as a plug flow and the variation in velocity is restricted to the air region around it. From these results we can also assume that we reach a mesh independent solution for the grid with $\Delta x = 0.0008$ *m*.

More interesting results are obtained when the profiles are plotted in a different dimensionless form. In a developed flow region the curve must present an self-similar shape in all the sections and it can be compared with the solutions of Wilcox [38](Fig. 7a) and Tollmien [1, 29](Fig. 7b). On both, the local velocity U is divided by the velocity on the jet axis U_x. The radial distance r is rendered dimensionless by dividing it by the vertical distance x for Wilcox profile and by dividing r by b for Tollmien solution, where b represents the value of r where the velocity is half of the velocity on the jet axis. Note that in a developing flow region $U_x = U_1$.

Figure 7 presents the fluid velocity profiles for horizontal profiles at distances $x = 0.8d_1$ to $x = 10.0d_1$ from the beginning of jet impact zone and the comparison with the solutions of Wilcox and Tollmien using mesh G0.0008. Since these solutions were derived to predict the velocities in the fully developed flow region [1], we must keep in mind that they will not necessarily correctly predict the flow at the jet beginning, and this is indeed what we find. From the analysis of Fig. 7a and Fig. 7b it can be noted that the profiles are converging to a self-similar solution, however, the first three profiles are quite a long way away from the fully developed solution, indicating that those are within the developing flow region and can not be used as a comparison. The true convergence and self-similarity was achieved slightly after $4.0d_1$, as is better shown in Fig. 7a. The profile at $x = 10.0d_1$ is shown not to converge on the approximation to the Tollmien solution at distances to the axis of the jet lower than $1.0r/b$ (Fig. 7b). At this depth the mesh is coarser and consequently the results are less accurate. The velocities plotted at profiles $x = 0.8d_1$ to $8.0d_1$ were evaluated in the refinement zone $Z1 - Z2$, whereas $10.0d_1$ were evaluated further down in the zone just covered by the refinement $Z2$ (Fig. 1).
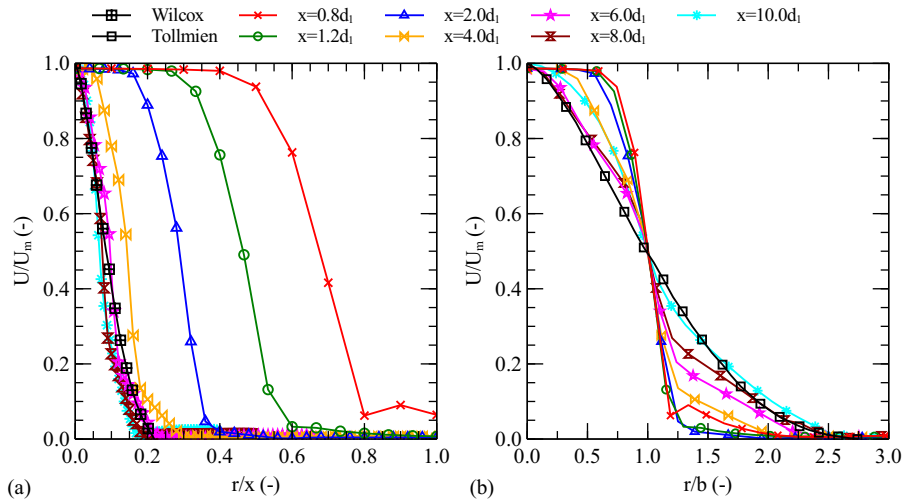
Figure 7. Liquid velocity profiles for some horizontal profiles along the pool depth ($x = 0.8d_1$ to $10.0d_1$). U_x is the velocity on the jet axis, x is the vertical direction and b the value of r where the velocity is half of the velocity on the jet axis. The profiles are compared with the solutions of (a) Wilcox and (b) Tollmien using mesh $G0.0008$

.

3.2.2. Free-surface detection and bubble formation

The dependence of the free-surface location on the α value and on the mesh refinement is shown in Fig. 8. Figure 8a shows the variation of the free-surface shape with α values on the finest mesh ($G0.0008$). Figure 8b shows the free-surface for different meshes keeping the value of alpha constant to 0.3.
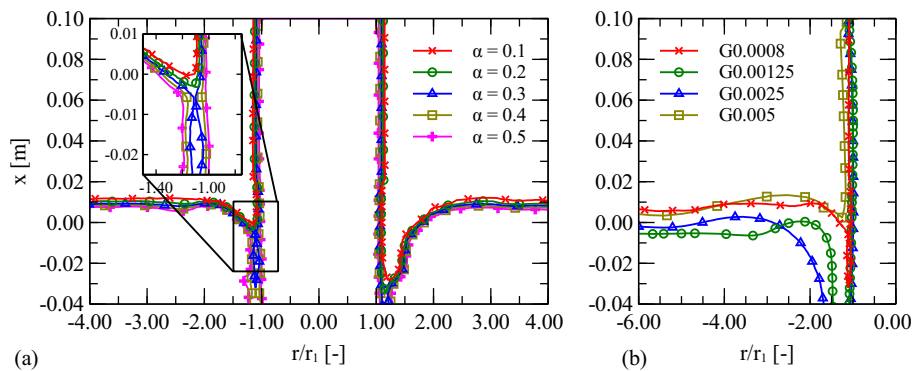

Figure 8. Temporal-averaged free-surface and air-cavity determined by: (a) keeping the finer mesh ($G0.0008$) and changing α value and (b) keeping $\alpha = 0.3$ and changing the mesh refinement. The x (m) axis is the vertical direction and r_1 (m) the jet radius at impact zone ($r_1 = 0.012$ m).

In a VOF simulation, the value of α that correctly represents the interface is not clearly defined; the interface is instead captured in the values between 0 and 1. Although some authors use a value of 0.5, the appropriate value should be subject of an analysis depending on the case under consideration. The α isosurface is strongly influenced

by turbulence at the free-surface and by what value of α we wish to consider as a threshold for the interface. Figure 8 shows the temporally averaged shape of the free-surface and the air cavity for various values of α. The overall shape of the free-surface (Fig. 8a) seems insensitive to the value of α used, however the cavity shape increases substantially in volume with increasing values of α. In fact, the interface fluctuations are higher in the air-cavities of the jet than in the remaining free-surface, making the value of α much more important in those regions.

Figure 8b presents the shape of the interface for the different levels of mesh refinement. The lack of cells in the coarser mesh produces a smoother connection between the pool free-surface and the jet, and neglects the creation of air cavities. In the other hand, the medium and fine mesh are able to generate and detect the cavities, however due to the lack of mesh resolution to calculate correctly the forces acting on the interface, the air cavity may not be formed correctly and closed, although we can see on the fine grid a smaller gap between the jet and the surface. At the end, the finest mesh has sufficient resolution to generate and close the cavities.

The effect of changing the mesh resolution is highly significant for the overall modelling of the entrainment process. As mentioned in the introduction, the whole entrainment process could be simulated by resolving the free-surface all the way to the scale of the entrained bubbles, however doing so would be phenomenally expensive and inappropriate for an engineering simulation. A more cost-effective approach would be to model the large scale shape of the free-surface on a relatively coarse mesh, with modelled entrainment into an Eulerian two-fluid model representing the statistical propagation of subgrid scale entrained bubbles. Technically speaking, for the Eulerian two-fluid model to work the bubble size should be substantially smaller than the cell size; however since the process of air-entrainment is a continuous one which is having to be truncated at some intermediate scale, it is likely that this constraint is being violated at some point.

The function E_g, representing the number of bubbles formed at the free-surface, is also presented in this section. Figure 9 shows the time-averaged values of E_g for the four meshes used and the free-surface position, delimited by ϕ_{FS} isolines of 0.1, 0.5 and 0.9. As mentioned before, a sharp interface is very important in order not to spread the E_g term over a large number of cells. In the first instance, observing Fig. 9, just the meshes $G0.0008$ and $G0.00125$ show E_g values calculated at the intersection of the jet with the pool, which is indeed the position where bubble formation was observed experimentally. However, our concern is also about the accuracy of E_g, and in these terms, $G0.0008$ mesh generates closest values when compared with the work of Ma et al. [23] and a more precise location of the zone of aeration – it can be noticed the generation of bubbles exactly inside of the air cavity, whereas in remaining meshes, E_g is spread all over the free-surface.

Figure 10 shows the comparison between the values of free-surface wave amplitude (*a*) using (a) the formulation of Ma et al. [23] and (b) the concept proposed in the current paper. Around the jet impact zone and inside the air cavity, the values are reasonably similar in both cases ($a \approx 0.001\ m$). These places, out of all the area occupied by the free-surface, are exactly the zones where the comparison should be made. The differences found at the centre of the jet has no importance for the calculation of E_g term and can be ignored.

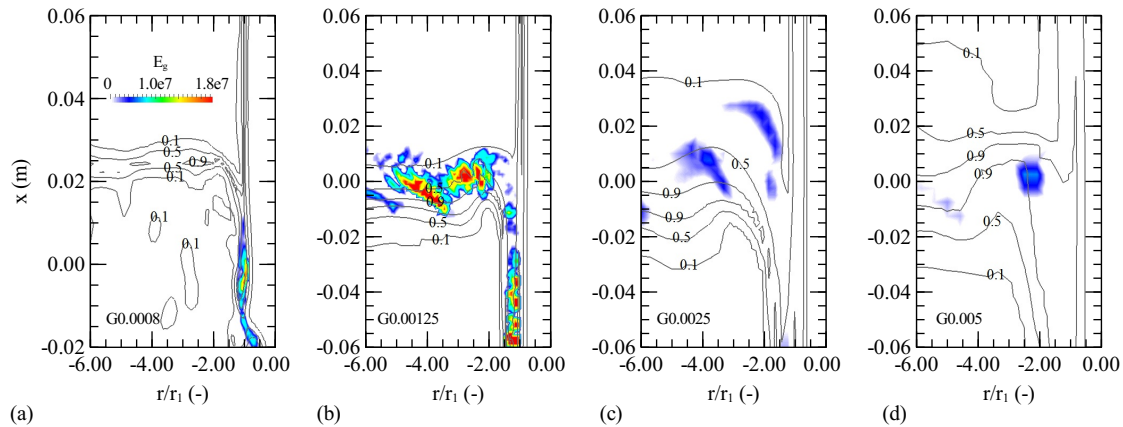Figure 9. 2D centre-slice profiles of the free-surface and bubble formation term using the meshes: (a) $G0.0008$, (b) $G0.00125$, (c) $G0.0025$ and (d) $G0.005$. Isolines correspond to ϕ_{FS} = 0.1, 0.5 and 0.9. The axis x is the vertical direction and r_1 the jet radius at impact zone (r_1 = 0.012 m).

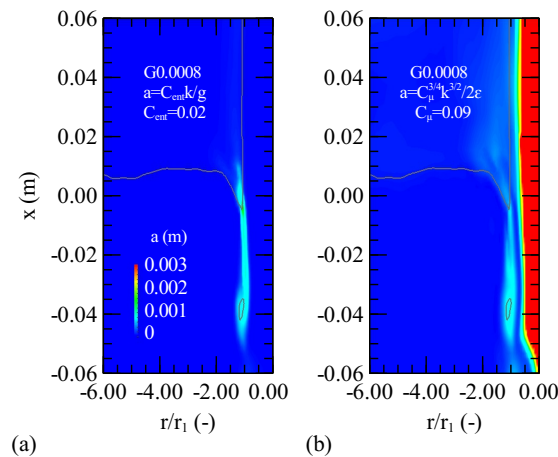Figure 10. Comparison between the value of free-surface wave amplitude (a) using (a) the formulation of Ma et al. [23] and (b) the concept proposed in this paper. The location of the free-surface is represented by $\alpha = 0.3$.

4. Conclusions

The present work attempts to numerically simulate air entrainment in two canonical cases; a 2D dam break and 3D circular plunging jet using Computational Fluid Dynamics. We investigate the interplay of numerical factors such as mesh resolution with the modelling processes of surface capturing and entrainment modelling. The VOF interface model as implemented in the code *interFoam* from the open-source OpenFOAM® toolkit was used to reproduce the interface between the water and air. In addition, an explicit term for air-entrainment detection was adapted to run with VOF models without a need of a calibration process. This was done by implementing a factor for free-surface detection and new concept of surface wave's amplitude based on the turbulent length scales.

The 2D dam break case was used to ascertain the influence of mesh size in the definition of free-surface position and aeration zone. The magnitude of air-entrainment term does not suffer much variation with the grid size, which let us believe that the new concept for wave's amplitude also improved the model on its independence of mesh size. The free-surface position is in contrast, much more sensible to the grid size and consequently a responsible to the accuracy of the aeration zone.

In the case of the 3D plunging jet, the free-surface shape was plotted using different mesh refinements and alpha values. The mesh refinement is shown to significantly affect the definition of the air cavities. The radial liquid velocity in the fully developed zone of the jet was found to be in reasonable agreement with analytical solution found on the literature. The term E_g for bubble formation reaches its maximum value in the intersection between the free-surface and the jet interface. This result is in agreement with visual descriptions of the air-entrainment process found in the literature. The term was successfully adapted to run within VOF based models and to be independent of user-calibration, by setting the free-surface wave's amplitude to be equal to the radius of the turbulent length scales. The results shown here prove that we might be optimistic about the applicability of this new concept, however, some other test cases are needed to validate the data as well as the conclusion of the air-entrainment model to compare the values of transported air.

5. Nomenclature

f   volumetric surface tension force, $kg\ m^{-2} s^{-2}$

g   gravity vector, $m\ s^{-2}$

n   free-surface normal vector, $-$

U   velocity vector, $m\ s^{-1}$

$\mathbf{U}_c$ compressive velocity, $m\ s^{-1}$

b value of r where the velocity is half of the velocity on the jet axis, m

C_α binary coefficient, $-$

C_μ turbulence model constant, $-$

C_{ent} constant for air-entrainment model, $-$

d jet diameter, m

E_g number of bubbles formed at free-surface, $m^{-3} s^{-1}$

g gravity, $m\ s^{-2}$

I turbulent intensity, $\%$

k turbulent kinetic energy, $m^2 s^{-2}$

l' turbulent length scale, m

p^* dynamic pressure, Pa or $kg\ m^{-1} s^{-2}$

r radial direction, jet radius, m

1	t	time, s
2	U	mean velocity, $m\ s^{-1}$
3	V_g	volume calculated assuming an averaged bubble diameter, m^3
4	x	vertical direction on pool, m
5	$Z1, Z2, Z3$	refinement zones of the mesh, $-$
6	*Greek Symbols*	
7	α	volume fraction, $-$
8	Δt	computational time step, s
9	κ	surface curvature, m^{-1}
10	μ	dynamic viscosity, $kg\ m^{-1}s^{-2}$
11	ν_t	turbulent viscosity, $m^2 s^{-1}$
12	ϕ_{ent}	interface thickness, m
13	ϕ_{FS}	interface location function, $-$
14	ρ	density, $kg\ m^{-3}$
15	σ	surface tension, $kg\ s^{-2}$
16	τ	shear stress tensor, Pa or $kg\ m^{-1}s^{-2}$
17	ε	turbulent dissipation, $m^2 s^{-3}$
18	n	water column width, m
19	*Subscripts*	
20	0	inlet position
21	1	jet impact position
22	$f1$	fluid 1
23	$f2$	fluid 2

5. Acknowledgments

References

[1] G. N. Abramovic. *The Theory of Turbulent Jets*. MIT Press, 1963.

[2] A. Baylar and M. E. Emiroglu. An experimental study of air entrainment and oxygen transfer at a water jet from a nozzle with air holes. *Water Environment Research*, 76(3):231–237, 2014.

[3] E. Berberović, N. P. van Hinsberg, S. Jakirlić, I. Roisman, and C. Tropea. Drop impact onto a liquid layer of finite thickness: Dynamics of the cavity evolution. *Physical Review E*, 79(3):1–15, 2009.

[4] A. K. Bin. Gas entrainment by plunging liquid jets. *Chemical Engineering Science*, 48(21):3585–3630, 1993.

[5] J. U. Brackbill, D. B. Kothe, and C. Zemach. A continuum method for modeling surface tension. *Journal of Computational Physics*, 100: 335–354, 1991.

[6] R. F. Carvalho, C. M. Lemos, and C. M. Ramos. Numerical computation of the flow in hydraulic jump stilling basins. *Journal of Hydraulic Research*, 46(6):739–752, 2008. doi: 10.3826/jhr.2008.2726.

[7] G. Cerne, S. Petelin, and I. Tiselj. Coupling of the interface tracking and the two-fluid models for the simulation of incompressible two-phase flow. *Journal of Computational Physics*, 171(2):776–804, 2001. ISSN 00219991. doi: 10.1006/jcph.2001.6810.

[8] H. Chanson. *Air Bubble Entrainment in Free-surface Turbulent Shear Flows*. Academic Press - Elsevier Ltd, 1996.

[9] H. Chanson and R. Manasseh. Air entrainment processes in a circular plunging jet: Void-fraction and acoustic measurements. *Journal of Fluids Engineering*, 125(5):910–921, 2003.

[10] H. Chanson, S. Aoki, and A. Hoque. Physical modelling and similitude of air bubble entrainment at vertical circular plunging jets. *Chemical Engineering Science*, 59(4):747–754, 2004.

[11] D. A. Drew and S. L. Passman. *Theory of Multicomponents Fluids*, volume 135. Springer, New York, USA, 1998. ISBN 0387983805.

[12] D. A. Ervine and H. T. Falvey. Behaviour of turbulent water jets in the atmosphere and in plunge pools. *Ice Proceedings*, 83(1):295–314, 1987. doi: 10.1680/iicep.1987.353.

[13] Fluent Inc. *Fluent 6.3 - User's Guide*. Fluent Inc., 2006.

[14] Susann Hänsch, Dirk Lucas, Eckhard Krepper, and Thomas Höhne. A multi-field two-fluid concept for transitions between different scales of interfacial structures. *International Journal of Multiphase Flow*, 47:171–182, 2012. doi: 10.1016/j.ijmultiphaseflow.2012.07.007.

[15] C. W. Hirt. Modeling turbulent entrainment of air at a free surface. Technical report, 2003.

[16] C. W. Hirt and B. D. Nichols. Volume of Fluid (VOF) method for the dynamics of free boundaries. *Journal of Computational Physics*, 39: 201–225, 1981.

[17] F. Z. Kendil, A. B. Salah, and A. Mataoui. Assessment of three turbulence model performances in predicting water jet flow plunging into a liquid pool. *Nuclear Technology and Radiation Protection*, 25(1):13–22, 2010.

[18] Kenneth T. Kiger and James H. Duncan. Air-entrainment mechanisms in plunging jets and breaking waves. *Annual Review of Fluid Mechanics*, 44(1):563–596, 2012. ISSN 0066-4189.

[19] J. Leandro, P. Lopes, R. F. Carvalho, P. Páscoa, R. Martins, and M. Romagnoli. Numerical and experimental characterization of the 2D vertical average-velocity plane at the centre-profile and qualitative air entrainment inside a gully for drainage and reverse flow. *Computers & Fluids*, 102:52–61, 2014.

[20] P. Lopes. *Free-surface flow interface and air-entrainment modelling using OpenFOAM*. PhD thesis, Thesis Project, University of Coimbra, 2013.

[21] P. Lopes, J. Leandro, R. F. Carvalho, P. Páscoa, and R. Martins. Numerical and experimental investigation of a gully under surcharge conditions. *Urban Water Journal*, 12(6):468–476, 2015. doi: 10.1080/1573062X.2013.831916.

[22] J. Ma, A. A. Oberai, D. A. Drew, R. T. Lahey Jr., and F. J. Moraga. A quantitative sub-grid air entrainment model for bubbly flows – plunging jets. *Computers & Fluids*, 39(1):77–86, 2010.

[23] J. Ma, A. A. Oberai, D. A. Drew, R. T. Lahey Jr., and M. C. Hyman. A comprehensive sub-grid air entrainment model for RaNS modeling of free-surface bubbly flows. *The Journal of Computational Multiphase Flows*, 3:41–56, 2011.

[24] A. Maiwald and R. Schwarze. Numerical analysis of flow-induced gas entrainment in roll coating. *Applied Mathematical Modelling*, 35(7): 3516–3526, 2011.

[25] H. Marschall and O. Hinrichsen. Numerical simulation of multi-scale two-phase flows using a hybrid interface - resolving two-fluid model (hires-tfm). *Journal of Chemical Engineering of Japan*, 46(8):517–523, 2013.

[26] E. J. McKeogh and D. A. Ervine. Air entrainment rate and diffusion pattern of plunging liquid jets. *Chemical Engineering Science*, 36: 1161–1172, 1981.

[27] Stephen B. Pope. *Turbulent Flows*. Cambridge University Press, 2000.

[28] X. L. Qu, L. Khezzar, D. Danciu, M. Labois, and D. Lakehal. Characterization of plunging liquid jets: A combined experimental and numerical investigation. *International Journal of Multiphase Flow*, 37(7):722–731, 2011.

[29] N. Rajaratnam. *Turbulent Jets*. Elsevier Scientific Publishing Company, 1976. ISBN 0-444-41372-3.

[30] W. J. Rider and D. B. Kothe. Reconstructing volume tracking. *Journal of Computational Physics*, 141(2):112–152, 1997.

[31] K. J. Sene. Air entrainment by plunging jets. *Chemical Engineering Science*, 43(10):2615–2623, 1988.

[32] J. A. Sethian. Fast marching methods. *SIAM Review*, 41:199–235, 1998.

[33] Olabanji Y Shonibare and Kent E Wardle. Numerical investigation of vertical plunging jet using a hybrid multifluid – VOF multiphase CFD solver. *International Journal of CHemical Engineering*, 2015(Article ID 925639):14, 2015. doi: 10.1155/2015/925639.

[34] O. Ubbink. *Numerical prediction of two fluid systems with sharp interfaces*. Phd thesis, Imperial College of Science, UK, 1997.

[35] H. K. Versteeg and W. Malalasekera. *An Introduction to Computational Fluid Dynamics - The Finite Volume Method*. Longman Scientific & Technical, 1995. ISBN 0-582-21884-5.

[36] K. E. Wardle and H. G. Weller. Hybrid multiphase CFD solver for coupled dispersed / segregated flows in liquid-liquid extraction. *International Journal of Chemical Engineering*, 2013.

[37] H. Weller. A new approach to VOF-based interface capturing methods for incompressible and compressible flows. *OpenCFD Ltd., Report TR/HGW/04*, 2008.

[38] D. C. Wilcox. *Turbulence Modeling for CFD*. DCW Industries, Inc., 1993. ISBN 0-9636051-0-0.

[39] K. Yan and D. Che. A coupled model for simulation of the gas – liquid two-phase flow with complex flow patterns. *International Journal of Multiphase Flow*, 36(4):333–348, 2010. ISSN 0301-9322. doi: 10.1016/j.ijmultiphaseflow.2009.11.007.

[40] Guan Heng Yeoh and Jiyuan Tu. *Computational Techniques for Multi-phase Flows*. Elsevier Ltd, 2010. ISBN 978-0-08046-733-7.